
Since January 2020 Elsevier has created a COVID-19 resource centre with free information in English and Mandarin on the novel coronavirus COVID-19. The COVID-19 resource centre is hosted on Elsevier Connect, the company's public news and information website.

Bioelectrochemistry 152 (2023) 108462

Contents lists available at ScienceDirect

Bioelectrochemistry

journal homepage: www.journals.elsevier.com/bioelectrochemistry

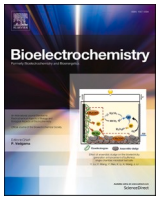

# A surface molecularly imprinted electrochemical biosensor for the detection of SARS-CoV-2 spike protein by using $Cu_7S_4$-Au as built-in probe

Zheng-Zhi Yin [a,*], Zixuan Liu [b], Min Zhou [c], Xu Yang [b], Guojun Zheng [c], Hongyu Zhang [c], Yong Kong [b,*]

[a] College of Biological, Chemical Sciences and Engineering, Jiaxing University, Jiaxing 314001, China
[b] Jiangsu Key Laboratory of Advanced Catalytic Materials and Technology, School of Petrochemical Engineering, Changzhou University, Changzhou 213164, China
[c] Department of Clinical Laboratory, Changzhou No.3 People's Hospital, Changzhou 213001, China

ARTICLE INFO

*Keywords:*
COVID-19
SARS-CoV-2 spike protein
Surface imprinting
Electrochemical biosensor
Built-in probe

ABSTRACT

Sensitive detection of severe acute respiratory syndrome coronavirus-2 (SARS-CoV-2) spike protein (S protein) is of significant clinical importance in the diagnosis of COVID-19 pandemic. In this work, a surface molecularly imprinted (SMI) electrochemical biosensor is fabricated for the detection of SARS-CoV-2 S protein. $Cu_7S_4$-Au is used as the built-in probe and modified on the surface of a screen-printed carbon electrode (SPCE). 4-Mercaptophenylboric acid (4-MPBA) is anchored to the surface of the $Cu_7S_4$-Au through Au–SH bonds, which can be used for the immobilization of the SARS-CoV-2 S protein template through boronate ester bonds. After that, 3-aminophenylboronic acid (3-APBA) is electropolymerized on the electrode surface and used as the molecularly imprinted polymers (MIPs). The SMI electrochemical biosensor is obtained after the elution of the SARS-CoV-2 S protein template with an acidic solution by the dissociation of the boronate ester bonds, which can be utilized for sensitive detection of the SARS-CoV-2 S protein. The developed SMI electrochemical biosensor displays high specificity, reproducibility and stability, which might be a potential and promising candidate for the clinical diagnosis of COVID-19.

## 1. Introduction

Since the outbreak of COVID-19 pandemic induced by severe acute respiratory syndrome coronavirus-2 (SARS-CoV-2) in 2019, it has brought about serious threats to global public health [1]. Therefore, the development of rapid analytical methods is of significant clinical importance for the diagnosis of COVID-19. Currently, reverse transcription-polymerase chain reaction (RT-PCR) is the popular diagnostic method for the detection of COVID-19 since viral RNA can be accurately identified by this method, however, large-scale application of RT-PCR is limited by its instrumentation costs, time-consuming analysis, and requirement of trained personnel.[2] In addition, it has been reported that due to the high sensitivity of RT-PCR to the fragments of viral RNA, the test for SARS-CoV-2 could be persistently positive up to 3 months in some individuals [2–4]. Recently, nucleocapsid protein (N protein) and spike protein (S protein) have been used as the antigen biomarkers for the accurate diagnosis of COVID-19 since the two immunodominant proteins in the virus can trigger dominant immune responses [5–7].

Because of the merits such as low cost, high sensitivity, and ease of operation, electrochemical biosensors can provide an alternative strategy for the clinical diagnosis of COVID-19 [8,9]. Molecularly imprinted electrochemical biosensors are a kind of special biosensors combining the specificity of molecularly imprinted polymers (MIPs) with the sensitivity of transducers, which have great potential for the diagnosis of infectious diseases [10,11]. Especially, the applications of MIPs-based electrochemical biosensors in the detection of SARS-CoV-2 S protein and N protein have been reported [1,12,13]. For instance, Ratautaite et al. [12] proposed molecularly imprinted polypyrrole, which acted as the MIPs and was successfully used in the detection of SARS-CoV-2 S protein by pulsed amperometric detection (PAD). However, conventional bulk imprinting is usually difficult to be applied for protein templates owing to the conformational change of proteins during the bulk imprinting process [14,15]. Surface imprinting, in which the templates are attached to the surface before polymerization, is especially suitable for protein templates, because it can minimize the aggregation of the templates and provide more accessible binding sites than bulk

* Corresponding authors.
*E-mail addresses:* yinzhengzhi@zjxu.edu.cn (Z.-Z. Yin), yzkongyong@cczu.edu.cn (Y. Kong).

https://doi.org/10.1016/j.bioelechem.2023.108462
Received 2 April 2023; Received in revised form 4 May 2023; Accepted 7 May 2023
Available online 10 May 2023

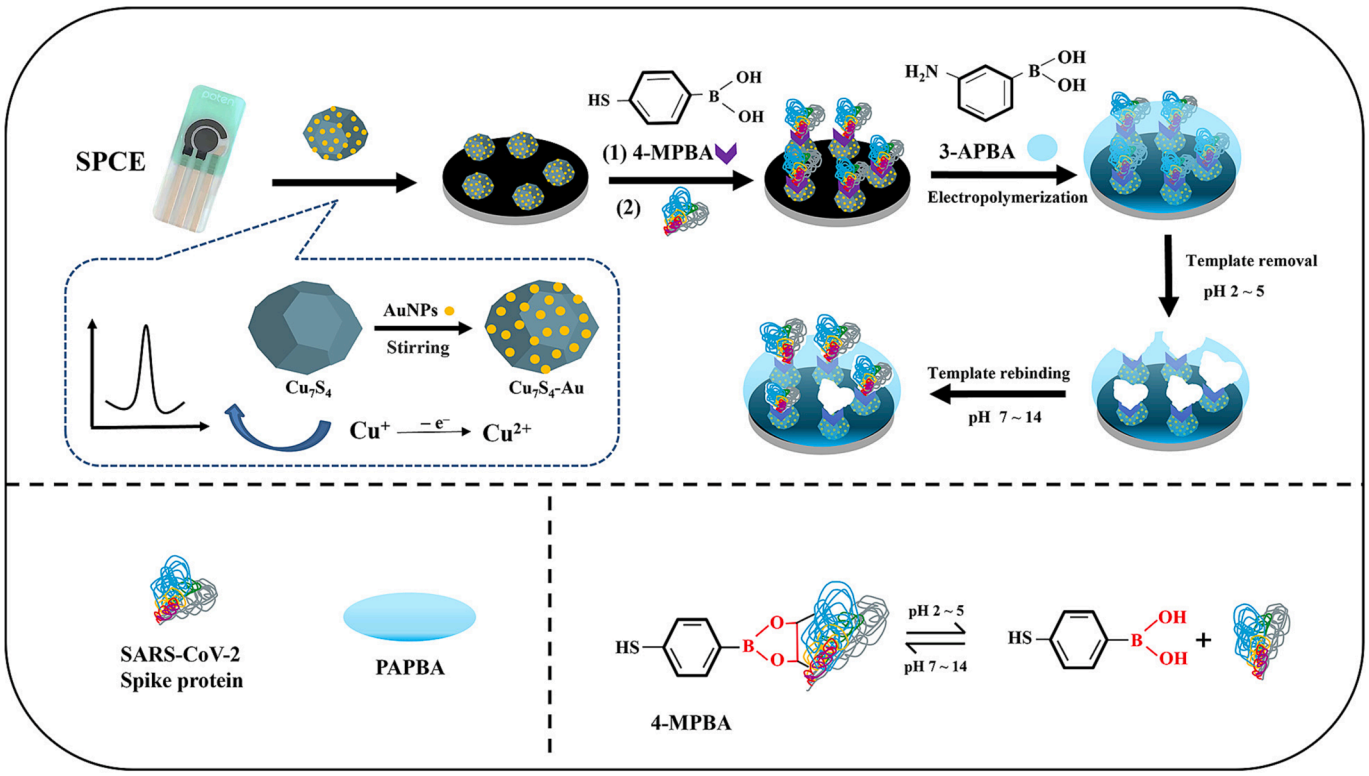


**Fig. 1.** Schematic diagram showing the fabrication of the SMI electrochemical biosensor.

imprinting [16,17].

Electron transfer mediators such as $K_3[Fe(CN)_6]$ [18], methylene blue (MB) [19], and toluidine blue (TB) [20] are commonly used as the signal indicators in electrochemical biosensors. Recently, copper sulfide ($Cu_xS_y$) nanocrystallites have attracted considerable attention as the signal probe for bioanalysis due to their high electrical conductivity, hypotoxicity, and peroxidase-mimicking activity [21,22]. More importantly, electrochemical signals can be easily produced through the electron transfer between $Cu^+$ and $Cu^{2+}$ in $Cu_xS_y$. However, little attention has been paid to the applications of $Cu_xS_y$ as the built-in probe in surface molecularly imprinted (SMI) electrochemical biosensors.

Herein, we report on the fabrication of a SMI electrochemical biosensor for the detection of SARS-CoV-2 S protein. Au nanoparticles (AuNPs) were anchored to the surface of $Cu_7S_4$ through the bonds of Au–S, and the resultant $Cu_7S_4$-Au was modified on the surface of a screen-printed carbon electrode (SPCE) and used as the built-in probe. The AuNPs can not only improve the sensitivity of the biosensor [22], but also connect with 4-mercaptophenylboric acid (4-MPBA) through Au–SH bonds. Because boric acid groups can covalently bind *cis*-diol groups of glycoproteins to form stable cyclic esters in neutral or alkaline media [23–25], the introduced 4-MPBA can be used for the immobilization of the SARS-CoV-2 S protein template through boronate ester bonds. After that, 3-aminophenylboronic acid (3-APBA) was electropolymerized on the surface by cyclic voltammetry and used as the MIPs. The SARS-CoV-2 S protein template was eluted with an acidic solution since the boronate ester bonds can be dissociated in acidic media [23–25], and thus the SMI electrochemical biosensor was obtained. Finally, the as-fabricated SMI electrochemical biosensor was used for the sensitive detection of SARS-CoV-2 S protein in solutions and clinical serum samples.

## 2. Experimental

### 2.1. Reagents and apparatus

Tetrachloroauric(III) acid trihydrate ($HAuCl_4{\cdot}3H_2O$), sodium hydroxide (NaOH), sodium fluoride (NaF), trisodium citrate, ascorbic acid, thiourea, aniline, concentrated sulfuric acid ($H_2SO_4$) and absolute ethanol were purchased from Sinopharm Chemical Reagent Co., Ltd. (Shanghai, China). Copper sulfate pentahydrate ($CuSO_4{\cdot}5H_2O$), 4-MPBA, 3-APBA, polyvinylpyrrolidone (PVP), bovine serum albumin (BSA) and hemoglobin (HGB) were obtained from Aladdin Chemical Reagent Co., Ltd. (Shanghai, China). IgG and IgM were received from Solarbio Technology Co., Ltd. (Beijing, China). Pyrrole was purchased from Shanghai Macklin Biochemical Technology Co., Ltd. (Shanghai, China), and SARS-CoV-2-S protein dissolved in 0.02 M PBS was received from Yibaixin Biotechnology Co., Ltd. (Hangzhou, China). The integrated three-electrode system including a SPCE (d = 5 mm) as working electrode, a Ag/AgCl electrode as reference electrode and a carbon electrode as counter electrode was obtained from Weihai Poten Technology Co., Ltd. (Weihai, China). All other reagents were of analytical grade and used as received. Three human serum samples were obtained from Changzhou No.3 People's Hospital, and the experiments involving them were carried out in line with the institutional guidelines of Jiaxing/Changzhou University and consent was obtained for their use from Changzhou No.3 People's Hospital. All aqueous solutions were prepared with ultrapure water (18.2 MΩ·cm) from a Milli-Q purification system (Merck, Germany).

Scanning electron microscopy (SEM) and elemental mapping characterization of $Cu_7S_4$ and $Cu_7S_4$-Au were conducted on a Sigma 500 scanning electron microscope (Zeiss, Germany) equipped with energy dispersive X-ray (EDX) spectrometer. Transmission electron microscopy (TEM) and the X-ray diffraction (XRD) characterization of $Cu_7S_4$ and $Cu_7S_4$-Au were conducted on a Tecnai G2 F20 transmission electron microscope (FEI, USA) and a D8 Advance diffractometer (Bruker, Germany), respectively. The X-ray photoelectron spectroscopy (XPS) of

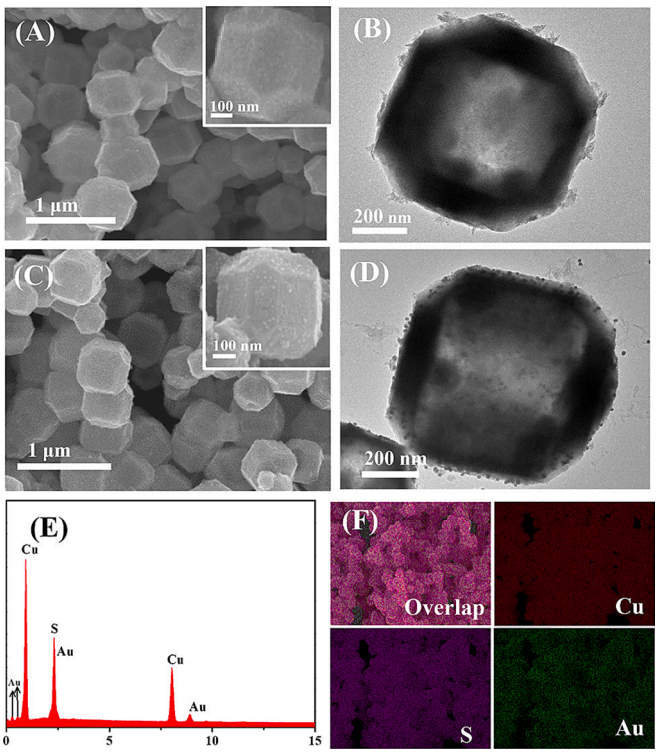


**Fig. 2.** SEM and TEM images of $Cu_7S_4$ (A, B) and $Cu_7S_4$-Au (C, D). EDX spectrum (E) and elemental mapping (F) of $Cu_7S_4$-Au.

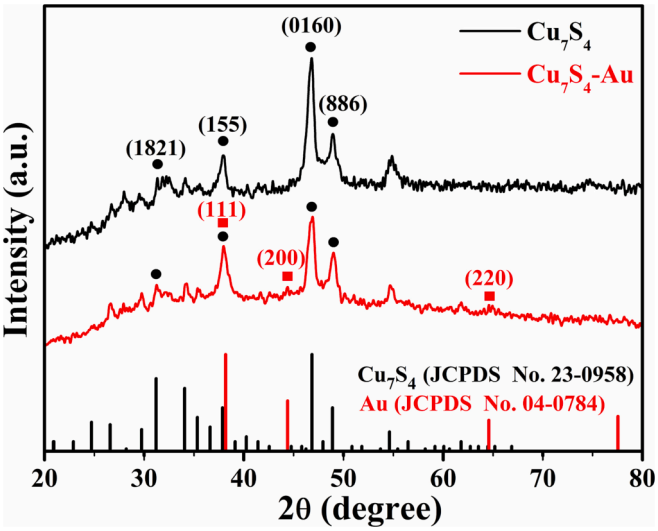


**Fig. 3.** XRD patterns of $Cu_7S_4$ and $Cu_7S_4$-Au.

$Cu_7S_4$-Au was investigated with an Axis Ultra DLD X-ray photoelectron spectrometer (Shimadzu, Japan). Atomic force microscopy (AFM) characterization of the SMI electrochemical biosensor was performed by means of a Dimension Icon microscope (Bruker, Germany). Water contact angles (2.0 μL stationary water droplets) on the surfaces of different samples were measured by using a DSA25 contact angle goniometer (Kruss GmbH, Germany). The differential pulse voltammograms (DPVs) and the electrochemical impedance spectroscopy (EIS) of different electrodes were acquired using a CHI 660E electrochemical workstation (Shanghai Chenhua Instruments Co., Ltd., China).

### 2.2. Synthesis of AuNPs and $Cu_7S_4$-Au

AuNPs were synthesized by the method previously reported [26]. In a typical procedure, 250 mL of $HAuCl_4$ aqueous solution (0.01 wt%) was brought to a boil with vigorous stirring, and then 3.75 mL of trisodium citrate aqueous solution (1 wt%) was added to this solution with a quick change of color from yellow to deep purple. Afterwards, the mixture was kept boiling for 10 min and then cooled down.

$Cu_7S_4$ was synthesized according to the previous literatures [22,27]. Briefly, 0.2 g of PVP was dissolved in 100 mL of 0.01 M $CuSO_4$ aqueous solution, and then 25 mL of 1.5 M NaOH solution was added to produce blue precipitates. After stirring for 1 min, 25 mL of 0.1 M ascorbic acid solution was added into the above mixture and continuously stirred for 15 min to produce a brick-red solution. Next, 5 mL of 0.2 M thiourea, which was used as the sulfur source, was added under heating conditions (90 °C) for 6 h. The black precipitates ($Cu_7S_4$) were centrifugally separated, washed, and vacuum-dried at 60 °C. After that, 10 mg of the $Cu_7S_4$ powder was added into 40 mL of the above AuNPs solution and stirred for 5 h, and the products of $Cu_7S_4$-Au were collected and vacuum-dried at 60 °C.

### 2.3. Immobilization of SARS-CoV-2 S protein template

The $Cu_7S_4$-Au was dispersed in water (2.5 mg $mL^{-1}$) under ultrasonication, and then 10 μL of the $Cu_7S_4$-Au dispersion was cast onto the SPCE surface and dried in ambient air. Next, 10 μL of absolute ethanol containing 0.1 M 4-MPBA was cast onto the surface of the $Cu_7S_4$-Au/SPCE and dried in ambient air for the anchoring of 4-MPBA through Au–SH bonds. Finally, 10 μL of 10 μg $mL^{-1}$ SARS-CoV-2-S protein (dissolved in 0.02 M PBS, pH = 7.4) was cast onto the surface of the MPBA/$Cu_7S_4$-Au/SPCE and incubated at 4 °C for 1 h, and the unbound SARS-CoV-2-S protein was washed away successively with 0.02 M PBS and water. The resultant electrode was denoted as S-protein/MPBA/$Cu_7S_4$-Au/SPCE.

### 2.4. Fabrication of SMI electrochemical biosensor

First, 100 μL of 0.1 M PBS (pH = 7.4) containing 40 mM 3-APBA and 40 mM NaF was cast onto the surface of the S-protein/MPBA/$Cu_7S_4$-Au/SPCE, and then the 3-APBA monomer was electropolymerized by cyclic voltammetry for consecutive 20 cycles in the potential range between –0.2 and 0.9 V (scan rate, 100 mV $s^{-1}$). After that, 100 μL of 0.2 M $H_2SO_4$ was cast onto the electrode surface and kept for 20 min to dissociate the boronate ester bonds and remove the SARS-CoV-2-S protein template. The SMI electrochemical biosensor was obtained after the de-doped SARS-CoV-2-S protein template was washed away with 0.1 M PBS (pH = 7.4). The schematic illustration of the fabrication of the SMI electrochemical biosensor is shown in Fig. 1.

For control experiments, the non-molecularly imprinted (NMI) electrochemical biosensor was also fabricated by the same procedures except for the addition of the SARS-CoV-2-S protein template.

### 2.5. Detection of SARS-CoV-2-S protein

The SMI electrochemical biosensor was incubated in 0.02 M PBS containing different concentrations of SARS-CoV-2-S protein for 30 min at 4 °C, and then the unbound protein was washed away with 0.1 M PBS of pH 7.4. The peak currents of the $Cu_7S_4$-Au built-in probe before and after the rebinding of the protein to the SMI electrochemical biosensor were monitored, and sensitive detection of the SARS-CoV-2-S protein can be achieved based on the decrease in the peak currents of the $Cu_7S_4$-Au built-in probe.

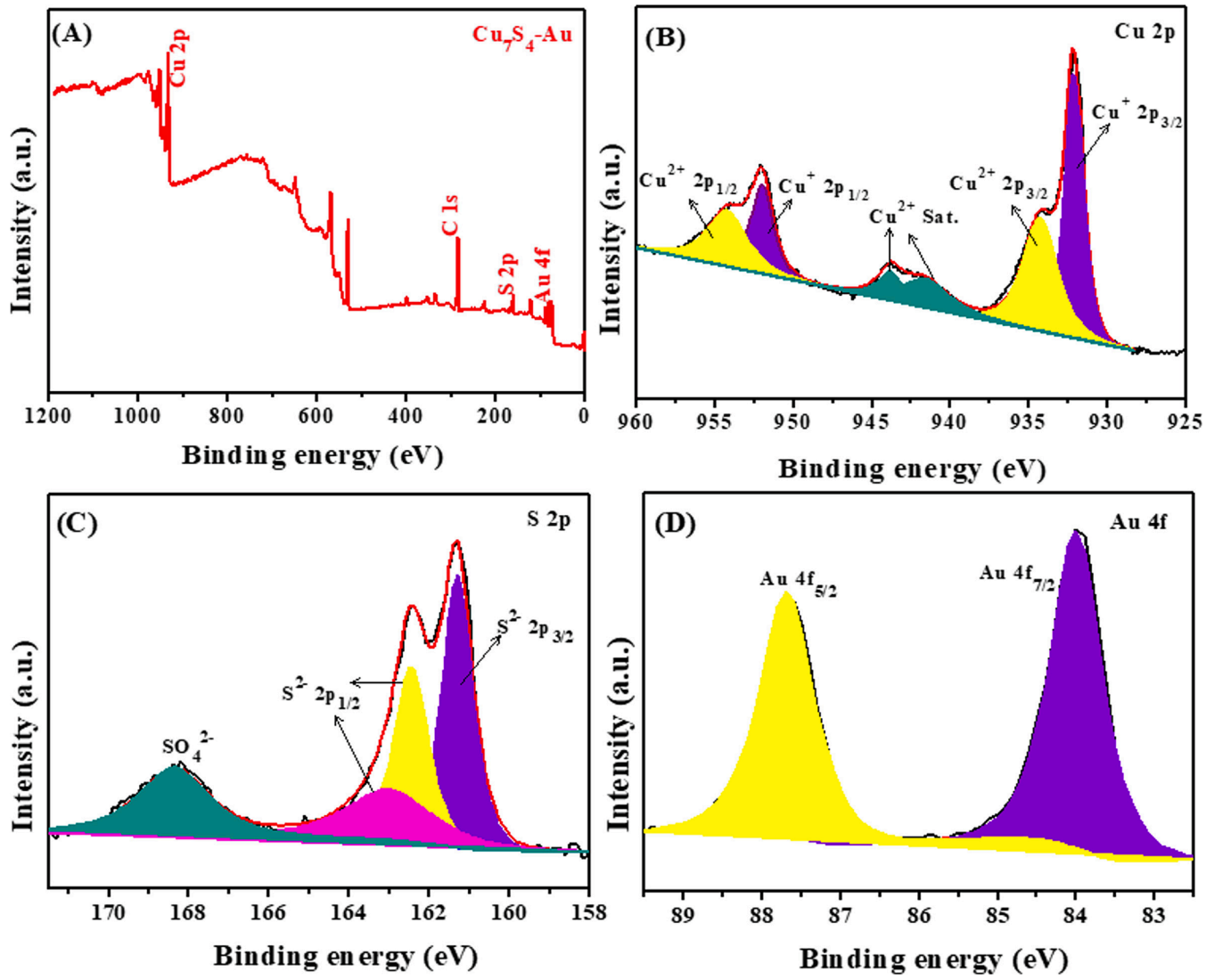


**Fig. 4.** XPS survey spectrum of $Cu_7S_4$-Au (A) and high-resolution XPS spectra for Cu 2p (B), S 2p (C) and Au 4f (D) of $Cu_7S_4$-Au.

## 3. Results and discussion

### 3.1. Morphologies and elemental mapping of $Cu_7S_4$ and $Cu_7S_4$-Au

The SEM and TEM images of $Cu_7S_4$ are presented in Fig. 2A and B, respectively. As can be seen, the as-synthesized $Cu_7S_4$ displays the morphology of regular hollow nanocages with an average size of ~ 600 nm. In the case of $Cu_7S_4$-Au, distinct AuNPs can be observed on the edges of the $Cu_7S_4$ nanocages (Fig. 2C and D), suggesting the anchoring of AuNPs to the surface of $Cu_7S_4$ through Au–S bonds. Both the EDX spectrum (Fig. 2E) and the elemental mapping (Fig. 2F) of the $Cu_7S_4$-Au reveal the existence of Cu, S and Au elements, further confirming the successful synthesis of the $Cu_7S_4$-Au built-in probe.

### 3.2. XRD patterns of $Cu_7S_4$ and $Cu_7S_4$-Au

The XRD patterns of $Cu_7S_4$ and $Cu_7S_4$-Au are shown in Fig. 3. The diffraction peaks of $Cu_7S_4$ located at $2\theta = 31.2°$, 36.6°, 46.8°, and 48.9° are consistent with the (1 8 2 1), (1 5 5), (0 1 6 0) and (8 8 6) planes of pure $Cu_7S_4$ (JCPDS No. 23-0958) [28,29]. After the anchoring of AuNPs through Au–S bonds, the diffraction peaks of $Cu_7S_4$ can still be observed on the XRD pattern of $Cu_7S_4$-Au at the same positions, indicating that the introduction of AuNPs does not alter the crystalline texture of $Cu_7S_4$. In addition, several new diffraction peaks appear at 38.2°, 44.4° and 64.6° on the XRD pattern of $Cu_7S_4$-Au, corresponding to the (1 1 1), (2 0 0) and (2 2 0) planes of Au, respectively [30]. This result further confirms the successful covalent anchoring of AuNPs to the $Cu_7S_4$ surface.

### 3.3. XPS analysis of $Cu_7S_4$-Au

Fig. 4A shows the XPS survey spectrum of the as-synthesized $Cu_7S_4$-Au. The four peaks located at 931.5, 283.1, 161.7 and 85.2 eV correspond to Cu 2p, C 1 s, S 2p and Au 4f, respectively. Among them, the C element might be originated from the reagents used for the synthesis of $Cu_7S_4$ (PVP, ascorbic acid and thiourea). The high-resolution XPS spectra of Cu 2p, S 2p and Au 4f are presented in Fig. 4B, C and D, respectively. The two main peaks centered at 934.3 and 954.1 eV on the Cu 2p spectrum correspond to $Cu^{2+}$ $2p_{3/2}$ and $Cu^{2+}$ $2p_{1/2}$, while another two main peaks at 932.1 and 951.9 eV are related to $Cu^{+}$ $2p_{3/2}$ and $Cu^{+}$ $2p_{1/2}$, respectively [31]. The double satellite peaks between the two pairs of main peaks are characteristic of $Cu^{2+}$, further confirming the co-existence of $Cu^{+}$ and $Cu^{2+}$ in the $Cu_7S_4$ [32,33]. The S 2p spectrum is divided into four peaks. The peak located at 161.3 eV corresponds to $S^{2-}$ $2p_{3/2}$, and the two peaks at 162.5 and 163.0 eV can be ascribed to $S^{2-}$ $2p_{1/2}$ [21]. Another peak at 168.4 eV is related to the residual $SO_4^{2-}$ species, which are associated with the oxidation of surface sulfur [22].

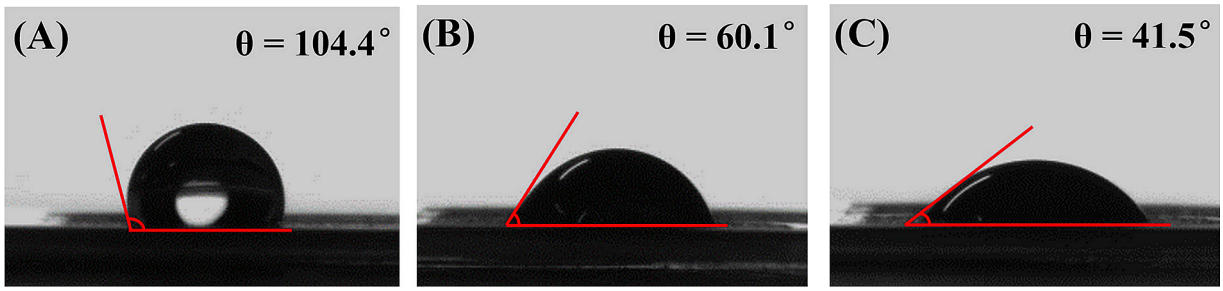


**Fig. 5.** Water contact angle values of SPCE (A), PAPBA coated electrode (B) and SMI electrochemical biosensor (C) with a representative picture.

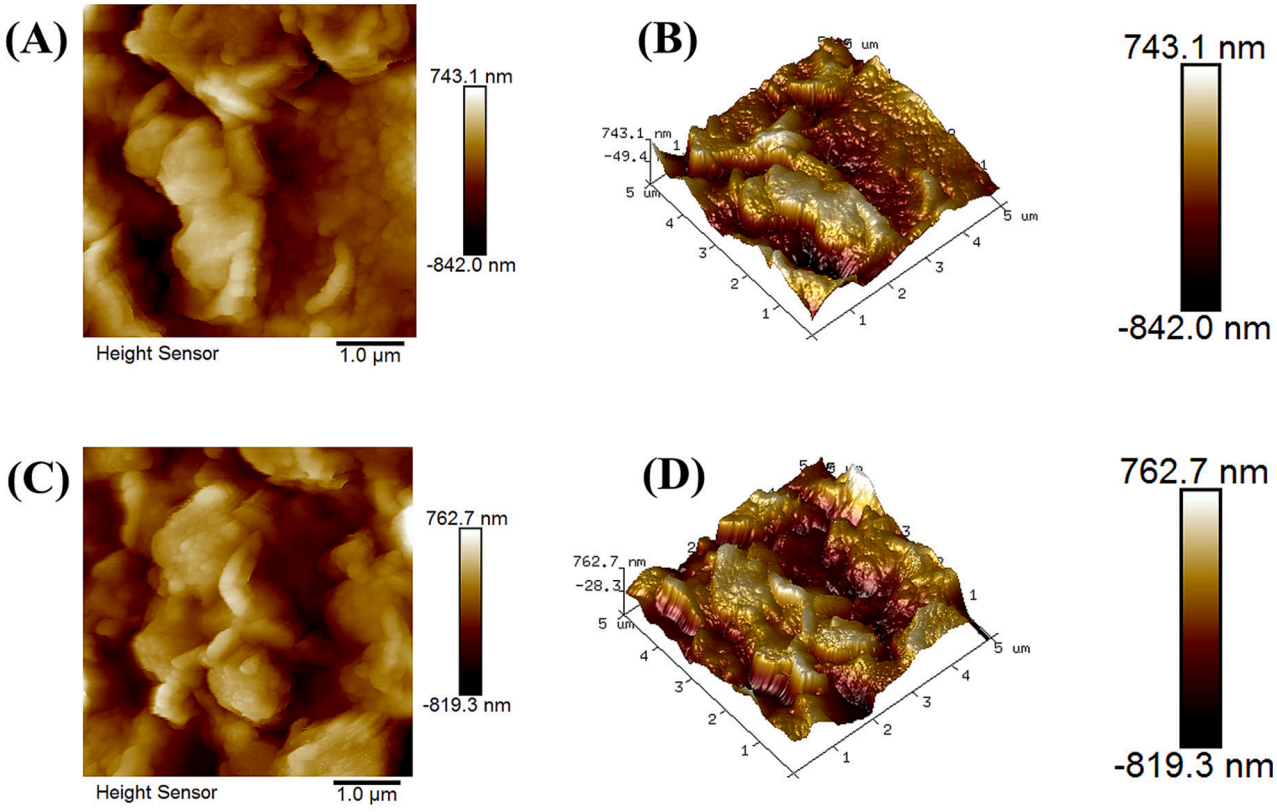


**Fig. 6.** Two- and three-dimensional AFM images of PAPBA coated electrode (A, B) and SMI electrochemical biosensor (C, D).

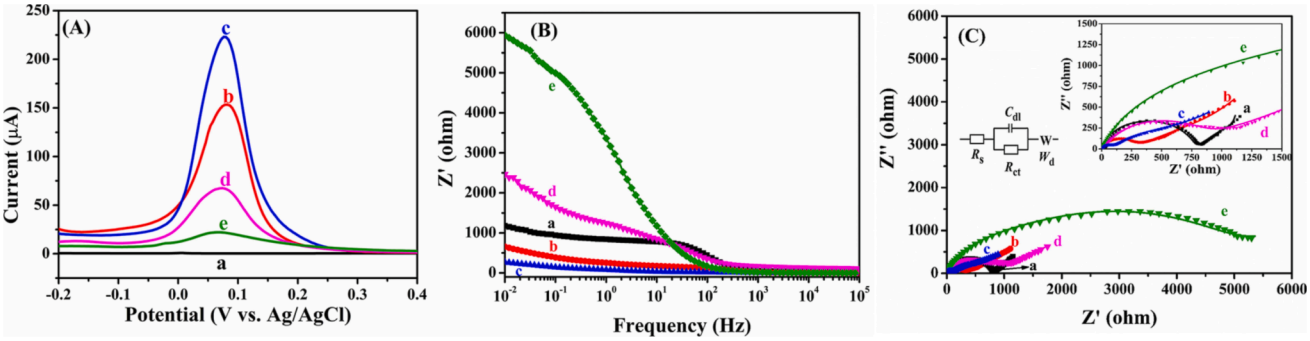


**Fig. 7.** DPVs (A), Bode (B) and Nyquist plots (C) of SPCE (a), $Cu_7S_4$/SPCE (b), $Cu_7S_4$-Au/SPCE (c), MPBA/$Cu_7S_4$-Au/SPCE (d) and S-protein/MPBA/$Cu_7S_4$-Au/SPCE (e) in 0.1 M PBS containing 0.1 M KCl. Frequency: $10^5 \sim 0.01$ Hz. Open circuit potential of EIS: 0.17 V. The Randles equivalent circuit in the inset of (B) is simulated by ZView software, where $R_s$ is the ohmic resistance of electrolyte and the internal resistance of electrode, $R_{ct}$ is the charge transfer resistance, $W_d$ is the Warburg resistance, and $C_{dl}$ is the double layer capacitance measured between the electrode and the electrolyte solution.

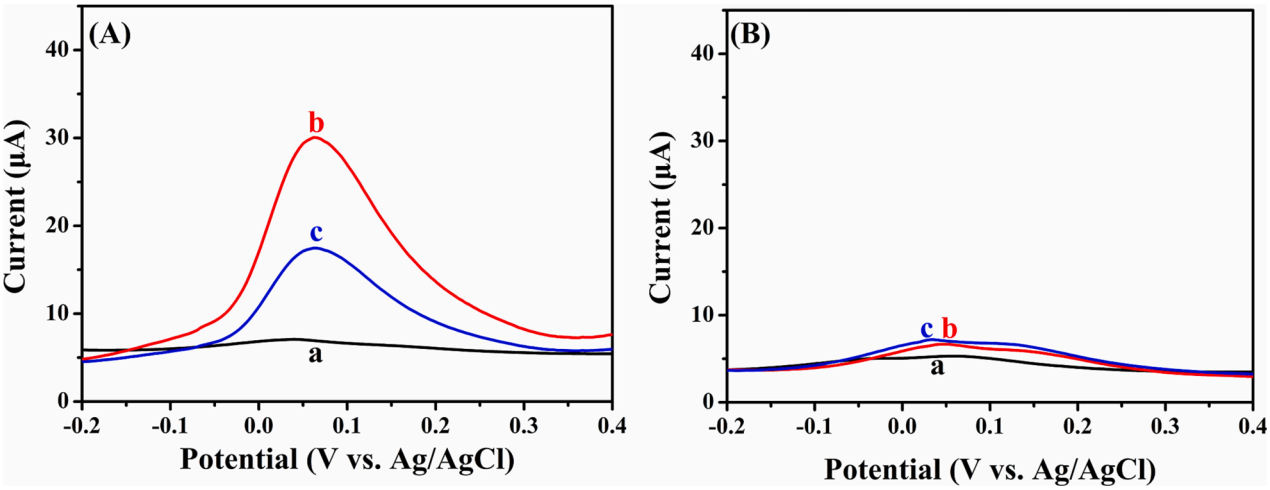


**Fig. 8.** (A) DPVs of PAPBA coated electrode (a), SMI biosensor before (a) and after (c) incubation in 0.02 M PBS (pH 7.4) containing 10 μg $mL^{-1}$ SARS-CoV-2-S protein. (B) DPVs of PAPBA coated electrode (a), NMI biosensor before (a) and after (c) incubation in 0.02 M PBS (pH 7.4) containing 10 μg $mL^{-1}$ SARS-CoV-2-S protein. Electrolyte: 0.1 M PBS containing 0.1 M KCl.

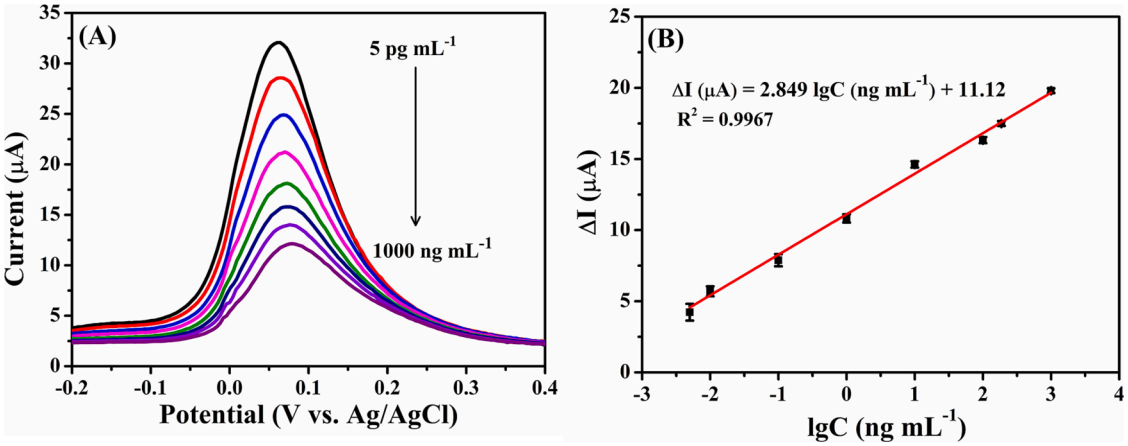


**Fig. 9.** (A) DPVs of the SMI biosensor after incubation in 0.02 M PBS containing different concentrations of SARS-CoV-2-S protein (0.005, 0.01, 0.1, 1, 10, 100, 500 and 1000 ng $mL^{-1}$) for 30 min. Electrolyte: 0.1 M PBS containing 0.1 M KCl. (B) Linear relationship between ΔI and lgC.

**Table 1**
Comparison of analytical performances between the developed SMI biosensor and other SARS-CoV-2-S protein biosensors.

| S protein biosensor | Linear range (ng $mL^{-1}$) | LOD (ng $mL^{-1}$) | Method | Reference |
|---|---|---|---|---|
| Magnet-assisted immunosensor | 0.01 ~ 1000 | 0.0072 | DPV | [6] |
| Self-assembled monolayer | — | 1109 | CV | [35] |
| | — | 872 | EIS | |
| Lateral flow device (LFD) | — | 5000 | LFD | [38] |
| Opto-microfluidic chip | — | 0.08 | LSPR | [39] |
| Electrochemical immunosensor | 40 ~ 10000 | 19 | DPV | [40] |
| SMI miniature biosensor | 0.1 ~ 1000 | 0.038 | SWV | [41] |
| SMI electrochemical biosensor | 0.005 ~ 1000 | 0.0017 | DPV | This work |

The Au 4f spectrum can be divided into two peaks at 84.0 and 87.7 eV, corresponding to Au $4f_{7/2}$ and Au $4f_{5/2}$, respectively, which are consistent with the chemical states of AuNPs [21].

### 3.4. Wettability evaluation of different samples

The wettability of different samples is evaluated to further understand the formation of the SMI electrochemical biosensor. As shown in Fig. 5A, the SPCE displays a high water contact angle (θ) of 104.4°, and the low hydrophilicity might be attributed to the absence of hydrophilic groups on the surface of the SPCE. After poly(3-APBA) (PAPBA) is electrodeposited on the electrode surface as the MIPs, the value of θ decreases greatly to 60.1° (Fig. 5B) due to the abundant hydrophilic groups (−$NH_2$ and − OH) of PAPBA. After the elution of the SARS-CoV-2-S protein template with $H_2SO_4$, the SMI electrochemical biosensor displays a further decreased θ of 41.5° (Fig. 5C). After the elution of the template, more hydrophilic groups of PAPBA are exposed to the electrode surface due to the formation of imprinted cavities within the PAPBA, which accounts for the enhanced hydrophilicity of the SMI electrochemical biosensor.

### 3.5. AFM images of PAPBA coated electrode and SMI electrochemical biosensor

The surface topographies of the PAPBA coated electrode and the SMI electrochemical biosensor are investigated by their two- and three-dimensional AFM images, in which the brighter and darker contrast

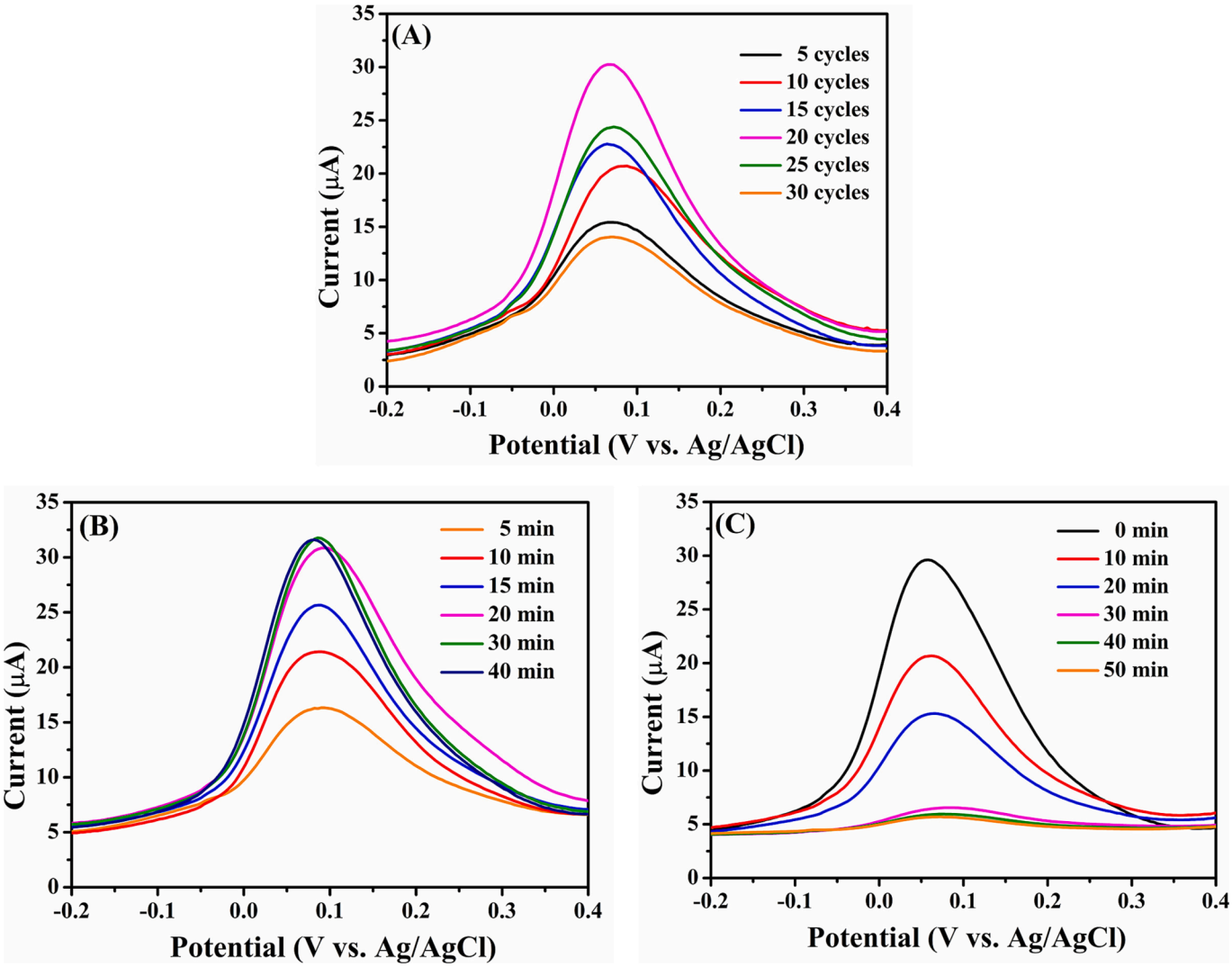


**Fig. 10.** Optimization of the cycling number for 3-APBA electropolymerization (A), elution time (B) and incubation time (C).

correspond to the higher and lower area of the surface, respectively. Compared with the PAPBA coated electrode (Fig. 6A and B), the SMI electrochemical biosensor exhibits a rougher surface (Fig. 6C and D). The root-mean-square (RMS) values of the PAPBA coated electrode and the SMI electrochemical biosensor are calculated to be 290.84 and 357.27 nm, respectively. As previously reported, the roughness of surfaces can be expressed in terms of RMS since the value of RMS is proportional to roughness [34]. Therefore, it can be concluded that the roughness of the SMI electrochemical biosensor is far higher than that of the PAPBA coated electrode, which might be caused by the successful removal of the SARS-CoV-2-S protein template from the PAPBA MIPs.

### 3.6. Electrochemical characterizations of different electrodes

The DPVs of different electrodes in 0.1 M PBS (pH = 7.4) containing 0.1 M KCl are shown in Fig. 7A. Compared with the SPCE (curve a), the $Cu_7S_4$/SPCE displays a distinct oxidation peak owing to the electron transfer from $Cu^+$ to $Cu^{2+}$ (curve b), suggesting that the $Cu_7S_4$ is a good built-in probe. The peak currents increase further at the $Cu_7S_4$-Au/SPCE (curve c), indicating that the AuNPs play an essential role in facilitating the electron transfer between $Cu^+$ and $Cu^{2+}$. After the introduction of electroinactive 4-MPBA through Au–SH bonds, the peak currents decrease remarkably at the MPBA/$Cu_7S_4$-Au/SPCE (curve d). The peak currents decrease further at the S-protein/MPBA/$Cu_7S_4$-Au/SPCE (curve e), which might be attributed to the low conductivity of the SARS-CoV-2-S protein. Successful step-by-step modification of the SPCE can also be confirmed by the results of EIS (Fig. 7B and C). Fig. 7B shows the Bode plots of different electrodes in the frequency ranging from $10^5$ Hz to 0.01 Hz. When the frequency is greater than 1000 Hz, there is no significant difference in the impedance values of these electrodes. The double-layer capacitance ($C_{dl}$) has greater impedance at lower frequencies [35,36]. Compared with SPCE (1178.2 Ω) and $Cu_7S_4$/SPCE (655.4 Ω), the impedance value of $Cu_7S_4$-Au/SPCE is reduced to 268.0 Ω at 0.01 Hz. After further introduction of electroinactive 4-MPBA and S protein, the impedance values increase significantly to 2465.2 Ω and 5938.9 Ω, respectively.

The charge transfer resistance ($R_{ct}$), which is denoted by the diameter of the suppressed semicircle in high frequency [37]. Fig. 7C shows the Nyquist plots of different electrodes in the frequency ranging from $10^5$ Hz to 0.01 Hz. Due to the excellent charge transfer ability of AuNPs, the $R_{ct}$ value of $Cu_7S_4$-Au/SPCE (59.6 Ω) is significantly smaller than those of SPCE (766.2 Ω) and $Cu_7S_4$/SPCE (258.9 Ω). The $R_{ct}$ values increase remarkably to 944.9 and 4855.0 Ω, respectively, after the introduction of 4-MPBA and S-protein. The results of the Nyquist plots are in line with those of the Bode plots, demonstrating successful step-by-step modification of the SPCE.

Fig. 8A shows the DPVs of the PAPBA coated electrode and the SMI biosensor before and after the incubation in 0.02 M PBS (pH 7.4)

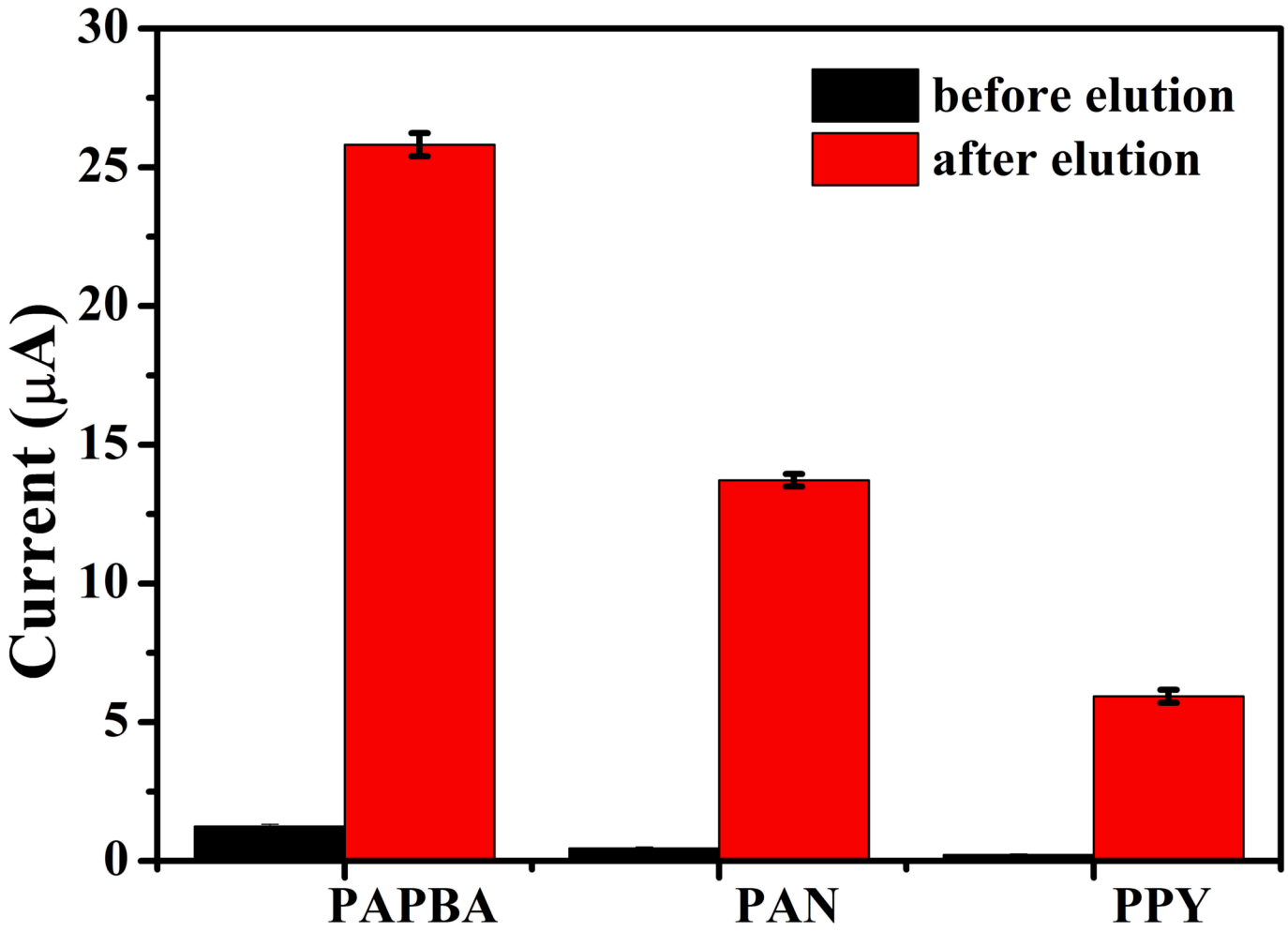


**Fig. 11.** The peak currents before and after the elution of the SARS-CoV-2 S protein template by using PAPBA, PAN and PPY as the MIPs, respectively. Electrolyte: 0.1 M PBS containing 0.1 M KCl.

containing 10 μg $mL^{-1}$ SARS-CoV-2-S protein. Compared with the S-protein/MPBA/$Cu_7S_4$-Au/SPCE (Fig. 7A, curve e), the peak currents at the PAPBA coated S-protein/MPBA/$Cu_7S_4$-Au/SPCE decrease further (curve a), which is most likely due to the low conductivity of PAPBA. After the treatment with 0.2 M $H_2SO_4$, the boronate ester bonds between the SARS-CoV-2-S protein template and the 4-MPBA is dissociated, leading to the removal of the template. As a result, the electron transfer is greatly facilitated by the generated imprinted cavities, resulting in significantly increased peak currents (curve b). However, the peak currents decrease again after the SMI biosensor is incubated in 0.02 M PBS containing 10 μg $mL^{-1}$ SARS-CoV-2-S protein (curve c), which might be ascribed to the rebinding of the SARS-CoV-2-S protein to the SMI biosensor though reversible boronate ester bonds. That is to say, the boronate ester bonds are dissociated in acid media (0.2 M $H_2SO_4$), while they can be formed again in neutral or alkaline media (0.02 M PBS of pH 7.4). In the case of the NMI biosensor (Fig. 8B), the peak currents vary little at different stages owing to the absence of the SARS-CoV-2-S protein template and the consequently generated imprinted cavities.

### 3.7. Detection of SARS-CoV-2-S protein with SMI biosensor

The as-fabricated SMI electrochemical biosensor is used for the detection of SARS-CoV-2-S protein. Fig. 9A shows the DPVs of the SMI biosensor after the incubation in 0.02 M PBS containing different concentrations of SARS-CoV-2-S protein for 30 min. As can be seen, the peak currents decrease gradually with increasing concentration of the SARS-CoV-2-S protein. When the concentration of the SARS-CoV-2-S protein is increased, the imprinted cavities within the PAPBA MIPs are gradually occupied by the protein through the reversible boronate ester bonds, resulting in suppressed electron transfer and the consequently decreased peak currents. As shown in Fig. 9B, there is a good linear relationship between the decrease in peak currents ($\Delta I$) and the logarithm value of the SARS-CoV-2-S protein concentration (lg$C$) in a wide concentration range from 5 pg $mL^{-1}$ to 1000 ng $mL^{-1}$, and the linear regression equation can be expressed as: $\Delta I$ (μA) = 2.849 lg$C$ (ng $mL^{-1}$) + 11.12 ($R^2$ = 0.9967). The limit of detection (LOD) is calculated to be 1.76 pg $mL^{-1}$ based on signal-to-noise ratio (S/N) of 3.

The analytical performances of the as-fabricated SMI biosensor are also compared with other SARS-CoV-2-S protein biosensors previously reported [6,35,38–41], and the results are listed in Table 1. Obviously, the developed SMI biosensor is far superior to the previous SARS-CoV-2-S protein biosensors in terms of both linear range and LOD.

### 3.8. Optimization of parameters

Several parameters influencing the sensitivity of the SMI electrochemical biosensor are optimized. The influence of the cycling number for 3-APBA electropolymerization on the peak currents of the SMI biosensor is presented in Fig. 10A. The peak currents increase with increasing cycling number till 20 cycles and then greatly decrease. The thickness of the resultant PAPBA MIPs is closely related to the cycling number. Inadequate cycling number results in a thin layer of the MIPs, which is associated with inadequate imprinted cavities; while excess cycling number may cause a thick layer of the MIPs, resulting in difficult

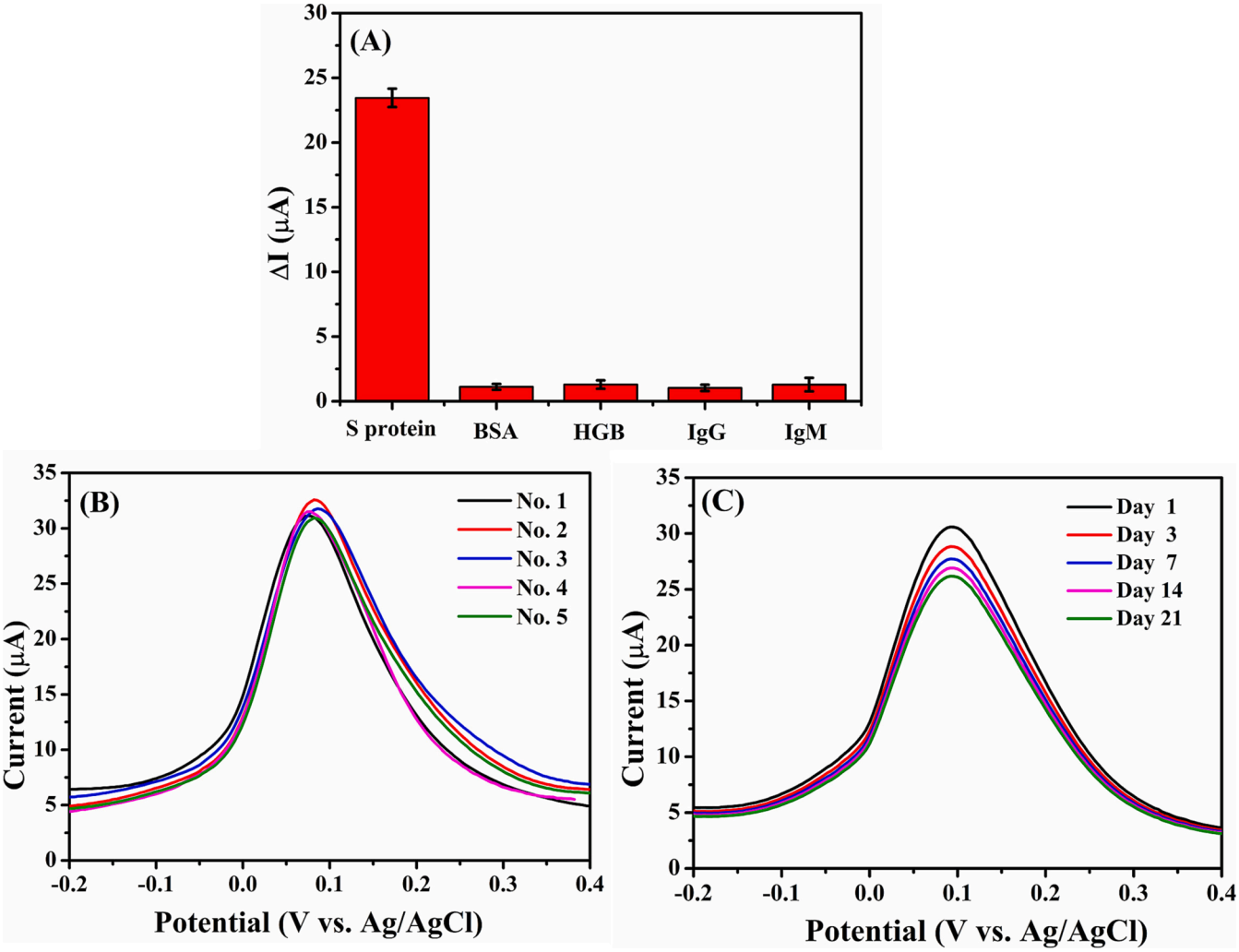


**Fig. 12.** Evaluation of specificity (A), reproducibility (B) and stability (C) of the developed SMI electrochemical biosensor.

elution of the SARS-CoV-2-S protein template. Therefore, 3-APBA is electropolymerized for 20 cycles as the MIPs. Fig. 10B shows the influence of elution time on the peak currents of the SMI biosensor. As can be seen, the peak currents vary little when the elution time exceeds 20 min, indicating that the template can be eluted completely from the MIPs in 20 min with 0.2 M $H_2SO_4$. Fig. 10C shows the influence of incubation time on the peak currents. It shows that the peak currents decrease gradually with increasing incubation time, with no further decrease from 30 min, suggesting that 30 min is enough for the imprinted cavities to be completely occupied by the SARS-CoV-2-S protein in the solution.

### 3.9. Selection of monomers used for the preparation of MIPs

Since aniline [42] and pyrrole [43] are two kinds of commonly used monomers used for the preparation of MIPs, the values of $\Delta I$ are compared by using polyaniline (PAN), polypyrrole (PPY) and PAPBA as the MIPs, respectively. Here, PAN and PPY were synthesized by electropolymerization of aniline and pyrrole, respectively [18,42]. Among the three MIPs, the value of $\Delta I$ using PAPBA MIPs is significantly larger than those using PAN and PPY MIPs (Fig. 11). Compared with PAN and PPY, the pronounced $\Delta I$ in the case of PAPBA MIPs might be due to the fact that besides 4-MPBA, PAPBA can also combine with the SARS-CoV-2 S protein template by boronate ester bonds, resulting in more imprinted cavities within the MIPs after the elution of the template.

### 3.10. Specificity, reproducibility and stability of SMI biosensor

To evaluate the quality of the developed SMI biosensor, specificity, reproducibility and stability are investigated. The values of $\Delta I$ before and after the incubation in 0.02 M PBS containing 10 μg $mL^{-1}$ BSA, HGB, IgG and IgM, which are possible co-existing substances, are negligible compared with that in the presence of SARS-CoV-2 S protein, even at the concentration of one percent of the interferents (100 ng $mL^{-1}$) (Fig. 12A), indicating excellent specificity of the SMI biosensor. The reproducibility of the SMI biosensor is also evaluated by recording the DPVs of five SMI biosensors fabricated under the same conditions. As shown in Fig. 12B, these DPVs are almost completely overlapped, and the relative standard deviation (RSD) of the peak currents is only 0.83%, suggesting high reproducibility of the SMI biosensor. The SMI biosensor is stored at 4 °C for three weeks, and the stability is evaluated by recording the DPVs at specific time intervals (Fig. 12C). After three weeks, the peak currents can still retain 81.10% of the initial value, indicating high stability of the SMI electrochemical biosensor.

### 3.11. Reliability of SMI biosensor

Finally, the reliability of the SMI electrochemical biosensor is assessed by the detection of SARS-CoV-2 S protein in three clinical serum samples by standard addition method. The small values of RSD (5.05%, 1.50% and 3.98%) (n = 3) as well as the narrow range of recovery (99.0% ~ 101.5%) demonstrate that the developed SMI electrochemical

biosensor is highly reliable.

## 4. Conclusions

In this work, a novel SMI electrochemical biosensor is developed for the detection of SARS-CoV-2-S protein. $Cu_7S_4$-Au is used as the built-in probe in the SMI biosensor and modified on the surface of the SPCE. 4-MPBA is anchored to the surface of the $Cu_7S_4$-Au through Au–SH bonds, which can be used for the capture of the SARS-CoV-2 S protein template via boronate ester bonds. 3-APBA is then electropolymerized on the electrode surface and the resultant PAPBA functions as the MIPs. After the elution of the SARS-CoV-2 S protein template with 0.2 M $H_2SO_4$ through the dissociation of the boronate ester bonds, the SMI biosensor is obtained, which can be utilized for the sensitive detection of SARS-CoV-2 S protein. The developed SMI biosensor displays high specificity, reproducibility and stability, and the reliability of the SMI biosensor is also demonstrated by the detection of SARS-CoV-2 S protein in clinical serum samples. These findings suggest that the developed SMI electrochemical biosensor might be a potential and promising candidate for the clinical diagnosis of COVID-19.

## Declaration of Competing Interest

The authors declare that they have no known competing financial interests or personal relationships that could have appeared to influence the work reported in this paper.

## Data availability

No data was used for the research described in the article.

## Acknowledgements

This work was supported by Technology Program of Zhejiang Province (LGF22B050008), Science and Technology Program of Jiaxing City (2022AY10012), Science and Technology Program of Changzhou City (CJ20220226) and Natural Science Foundation for Colleges and Universities in Jiangsu Province (20KJA150005).

## References

[1] V. Ratautaite, R. Boguzaite, E. Brazys, A. Ramanaviciene, E. Ciplys, M. Juozapaitis, R. Slibinskas, M. Bechelany, A. Ramanavicius, Molecularly imprinted polypyrrole based sensor for the detection of SARS-CoV-2 spike glycoprotein, Electrochim. Acta 403 (2022), 139581.
[2] A.G. Ayankojo, R. Boroznjak, J. Reut, A. Opik, V. Syritski, Molecularly imprinted polymer based electrochemical sensor for quantitative detection of SARS-CoV-2 spike protein, Sens. Actuators, B 353 (2022), 131160.
[3] C.H. Hernando, J.A.A. Serra, M.J.E. Saco, S. Martinez-Nadal, C.V. Ceren, PCR test for SARS-CoV-2 persistently positive. Virus detection is not always COVID-1, An. Pediatr. 93 (2020) 264–265.
[4] A. Wajnberg, M. Mansour, E. Leven, N.M. Bouvier, G. Patel, A. Firpo-Betancourt, R. Mendu, J. Jhang, S. Arinsburg, M. Gitman, J. Houldsworth, E. Sordillo, A. Paniz-Mondolfi, I. Baine, V. Simon, J. Aberg, F. Krammer, D. Reich, C. Cordon-Cardo, Humoral response and PCR positivity in patients with COVID-19 in the New York City region, USA: An observational study, Lancet Microbe 1 (2020) E283–E289.
[5] A. Rump, R. Risti, M.L. Kristal, J. Reut, V. Syritski, A. Lookene, S.R. Boudinot, Dual ELISA using SARS-CoV-2 nucleocapsid protein produced in E. coli and CHO cells reveals epitope masking by N-glycosylation, Biochem. Biophys. Res. Commun. 534 (2021) 457–460.
[6] J.L. Zhao, F. Zhao, H.L. Li, Y.L. Xiong, S.F. Cai, C. Wang, Y.F. Chen, N. Han, R. Yang, Magnet-assisted electrochemical immunosensor based on surface-clean Pd-Au nanosheets for sensitive detection of SARS-CoV-2 spike protein, Electrochim. Acta 404 (2022), 139766.
[7] M.L. Zhang, X.D. Li, J.L. Pan, Y.L. Zhang, L. Zhang, C.G. Wang, X. Yan, X.M. Liu, G. Y. Lu, Ultrasensitive detection of SARS-CoV-2 spike protein in untreated saliva using SERS-based biosensor, Biosens. Bioelectron. 190 (2021), 113421.
[8] H. Zhao, F. Liu, W. Xie, T.C. Zhou, J. OuYang, L. Jin, H. Li, C.Y. Zhao, L. Zhang, J. Wei, Y.P. Zhang, C.P. Li, Ultrasensitive supersandwich-type electrochemical sensor for SARS-CoV-2 from the infected COVID-19 patients using a smartphone, Sens. Actuators, B 327 (2021), 128899.
[9] A.K. Kaushik, J.S. Dhau, H. Gohel, Y.K. Mishra, B. Kateb, N.Y. Kim, D.Y. Goswami, Electrochemical SARS-CoV-2 sensing at point-of-care and artificial intelligence for intelligent COVID-19 management, ACS Appl. Bio Mater. 3 (2020) 7306–7325.
[10] M.A. Tabrizi, J.P. Fernandez-Blazquez, D.M. Medina, P. Acedo, An ultrasensitive molecularly imprinted polymer-based electrochemical sensor for the determination of SARS-CoV-2-RBD by using macroporous gold screen-printed electrode, Biosens. Bioelectron. 196 (2022), 113729.
[11] F.Y. Cui, Z.R. Zhou, H.S. Zhou, Molecularly imprinted polymers and surface imprinted polymers based electrochemical biosensor for infectious diseases, Sensors 20 (2020) 996.
[12] V. Ratautaite, R. Boguzaite, E. Brazys, D. Plausinaitis, S. Ramanavicius, U. Samukaite-Bubniene, M. Bechelany, A. Ramanavicius, Evaluation of the interaction between SARS-CoV-2 spike glycoproteins and the molecularly imprinted polypyrrole, Talanta 253 (2023), 123981.
[13] S. Ramanavicius, A. Ramanavicius, Development of molecularly imprinted polymer based phase boundaries for sensors design (review), Adv. Colloid Interface Sci. 305 (2022), 102693.
[14] S.S. Wang, J. Ye, Z.J. Bie, Z. Liu, Affinity-tunable specific recognition of glycoproteins via boronate affinity-based controllable oriented surface imprinting, Chem. Sci. 5 (2014) 1135–1140.
[15] A.X. Liang, S.S. Tang, M. Liu, Y. Yi, B.T. Xie, H.P. Hou, A.Q. Luo, A molecularly imprinted electrochemical sensor with tunable electrosynthesized Cu-MOFs modification for ultrasensitive detection of human IgG, Bioelectrochemistry 146 (2022), 108154.
[16] M. Torkashvand, M.B. Gholivand, G. Malekzadeh, Construction of a new electrochemical sensor based on molecular imprinting recognition sites on multiwall carbon nanotube surface for analysis of ceftazidime in real samples, Sens. Actuators, B 231 (2016) 759–767.
[17] Z.X. Liu, Z.Z. Yin, G.J. Zheng, H.Y. Zhang, M. Zhou, S. Li, Y. Kong, Dual-template molecularly imprinted electrochemical biosensor for IgG-IgM combined assay based on a dual-signal strategy, Bioelectrochemistry 148 (2022), 108267.
[18] Z.X. Liu, Z.Z. Yin, W.R. Cai, D.T. Wu, J.Y. Li, Y. Kong, A surface protein-imprinted biosensor based on boronate affinity for the detection of anti-human immunoglobulin G, Microchim. Acta 189 (2022) 106.
[19] P.J. Jing, C.Q. Zhao, Z.Z. Yin, B.Z. Yang, J.Y. Li, W.R. Cai, Y. Kong, An electrochemical chiral sensor based on competitive host-guest interaction for the discrimination of electroinactive amino acids, Analyst 147 (2022) 5068–5074.
[20] Y.C. Wei, H.M. Ma, X. Ren, C.F. Ding, H. Wang, X. Sun, B. Du, Y. Zhang, Q. Wei, A dual-signaling electrochemical ratiometric method for sensitive detection of carcinoembryonic antigen based on Au-$Cu_2S$-CuS/graphene and Au-$CeO_2$ supported toluidine blue complex, Sens. Actuators, B 256 (2018) 504–511.
[21] Y.R. Qian, Y. Du, J.H. Feng, R. Xu, X. Ren, D.W. Fan, Q. Wei, H.X. Ju, A duple nanozyme stimulating tandem catalysis assisted multiple signal inhibition strategy for photoelectrochemical bioanalysis, Sens. Actuators, B 334 (2021), 129608.
[22] Y.Y. Li, W.J. Zhu, Q. Kang, L. Yang, Y. Zhang, Y.G. Wang, Q. Wei, Dual-mode electrochemical immunoassay for insulin based on $Cu_7S_4$-Au as a double signal indicator, ACS Appl. Mater. Interfaces 10 (2018) 38791–38798.
[23] L. Li, Y. Lu, Z.J. Bie, H.Y. Chen, Z. Liu, Photolithographic boronate affinity molecular imprinting: a general and facile approach for glycoprotein imprinting, Angew. Chem. Int. Ed. 52 (2013) 7451–7454.
[24] R.R. Xing, S.S. Wang, Z.J. Bie, H. He, Z. Liu, Preparation of molecularly imprinted polymers specific to glycoproteins, glycans and monosaccharides via boronate affinity controllable-oriented surface imprinting, Nat. Protoc. 12 (2017) 964–987.
[25] M. You, S. Yang, W.X. Tang, F. Zhang, P.G. He, Ultrasensitive electrochemical detection of glycoprotein based on boronate affinity sandwich assay and signal amplification with functionalized $SiO_2$@Au nanocomposites, ACS Appl. Mater. Interfaces 9 (2017) 13855–13864.
[26] X.N. Zhang, C.Y. Huang, Y.X. Jiang, J.Z. Shen, P. Geng, W. Zhang, Q.L. Huang, An electrochemical glycan biosensor based on a thionine-bridged multiwalled carbon nanotube/gold nanoparticle composite-modified electrode, RSC Adv. 6 (2016) 112981–112987.
[27] H.L. Cao, X.F. Qian, C. Wang, X.D. Ma, J. Yin, Z.K. Zhu, High symmetric 18-facet polyhedron nanocrystals of $Cu_7S_4$ with a hollow nanocage, J. Am. Chem. Soc. 127 (2005) 16024–16025.
[28] H.J. Zhao, T.T. Liu, L. Cui, Y.H. Li, F. Yang, X.M. Zhang, Label-free and dual-amplified electrochemical bioanalysis of MUC1 based on an inorganic-organic polymer hybrid mimic peroxidase (AuNPs@$Cu_7S_4$@Cu/Mn-AzoPPOP) and catalytic hairpin assembly, Sens. Actuators, B 345 (2021), 130332.
[29] H.J. Gao, Y.J. Chen, H.L. Li, F.F. Zhang, G.H. Tian, Hierarchical $Cu_7S_4$-$Cu_9S_8$ heterostructure hollow cubes for photothermal aerobic oxidation of amines, Chem. Eng. J. 363 (2019) 247–258.
[30] J.B. Cui, R. Jiang, C. Guo, X.L. Bai, S.Y. Xu, L.Y. Wang, Fluorine grafted $Cu_7S_4$-Au heterodimers for multimodal imaging guided photothermal therapy with high penetration depth, J. Am. Chem. Soc. 140 (2018) 5890–5894.
[31] M.R. Wang, F. Xie, W.J. Li, M.F. Chen, Y. Zhao, Preparation of various kinds of copper sulfides in a facile way and the enhanced catalytic activity by visible light, J. Mater. Chem. A 1 (2013) 8616–8621.
[32] J. Xu, J.B. Cui, C. Guo, Z.P. Zhao, R. Jiang, S.Y. Xu, Z.B. Zhuang, Y. Huang, L. Y. Wang, Y.D. Li, Ultrasmall $Cu_7S_4$@$MoS_2$ hetero-nanoframes with abundant active edge sites for ultrahigh-performance hydrogen evolution, Angew. Chem. Int. Ed. 55 (2016) 6502–6505.
[33] D. Kelly, A. Singh, C.A. Barrett, C. O'Sullivan, C. Coughlan, F.R. Laffir, C. O'Dwyer, K.M. Ryan, A facile spin-cast route for cation exchange of multilayer perpendicularly-aligned nanorod assemblies, Nanoscale 3 (2011) 4580–4583.

[34] K. Kor, K. Zarei, Development and characterization of an electrochemical sensor for furosemide detection based on electropolymerized molecularly imprinted polymer, Talanta 146 (2016) 181–187.
[35] M. Drobysh, V. Liustrovaite, A. Baradoke, A. Rucinskiene, A. Ramanaviciene, V. Ratautaite, R. Viter, C.F. Chen, I. Plikusiene, U. Samukaite-Bubniene, R. Slibinskas, E. Ciplys, M. Simanavicius, A. Zvirbliene, I. Kucinskaite-Kodze, A. Ramanavicius, Electrochemical determination of interaction between SARS-CoV-2 spike protein and specific antibodies, Int. J. Mol. Sci. 23 (2022) 6768.
[36] V. Liustrovaite, M. Drobysh, A. Rucinskiene, A. Baradoke, A. Ramanaviciene, I. Plikusiene, U. Samukaite-Bubniene, R. Viter, C.F. Chen, A. Ramanavicius, Towards an electrochemical immunosensor for the detection of antibodies against SARS-CoV-2 spike protein, J. Electrochem. Soc. 169 (2022), 037523.
[37] H.L. Ge, Y. Kong, Y. Pan, L.H. Deng, D. Shou, Q.Y. Lu, Polydopamine core half-polyamidoamine dendrimers based drug-delivery platform and characterization by electrochemical impedance spectroscopy, J. Electrochem. Soc. 162 (2015) G87–G93.
[38] A.N. Baker, S.J. Richards, C.S. Guy, T.R. Congdon, M. Hasan, A.J. Zwetsloot, A. Gallo, J.R. Lewandowski, P.J. Stansfeld, A. Straube, M. Walker, S. Chessa, G. Pergolizzi, S. Dedola, R.A. Field, M.I. Gibson, The SARS-COV-2 spike protein binds sialic acids and enables rapid detection in a lateral flow point of care diagnostic device, ACS Cent. Sci. 6 (2020) 2046–2052.
[39] R. Funari, K.Y. Chu, A.Q. Shen, Detection of antibodies against SARS-CoV-2 spike protein by gold nanospikes in an opto-microfluidic chip, Biosens. Bioelectron. 169 (2020), 112578.
[40] L. Fabiani, M. Saroglia, G. Galata, R. De Santis, S. Fillo, V. Luca, G. Faggioni, N. D'Amore, E. Regalbuto, P. Salvatori, G. Terova, D. Moscone, F. Lista, F. Arduini, Magnetic beads combined with carbon black-based screen-printed electrodes for COVID-19: A reliable and miniaturized electrochemical immunosensor for SARS-CoV-2 detection in saliva, Biosens. Bioelectron. 171 (2021), 112686.
[41] X. Yang, Z.Z. Yin, G.J. Zheng, M. Zhou, H.Y. Zhang, J.Y. Li, W.R. Cai, Y. Kong, Molecularly imprinted miniature electrochemical biosensor for SARS-CoV-2 spike protein based on Au nanoparticles and reduced graphene oxide modified acupuncture needle, Bioelectrochemistry 151 (2023), 108375.
[42] M.R. Moghadam, L. Salehi, S. Jafari, N. Nasirizadeh, J. Ghasemi, Voltammetric sensing of oxacillin by using a screen-printed electrode modified with molecularly imprinted polyaniline, gold nanourchins and graphene oxide, Microchim. Acta 186 (2019) 798.
[43] Q.Q. Zhao, J.P. Yang, J. Zhang, D.T. Wu, Y.X. Tao, Y. Kong, Single-template molecularly imprinted chiral sensor for simultaneous recognition of alanine and tyrosine enantiomers, Anal. Chem. 91 (2019) 12546–12552.